Simultaneous measurement of flame temperature and absorption coefficient through LMBC-NNLS and plenoptic imaging techniques

Jian Li[1], Md. Moinul Hossain[2], Jun Sun[3], Yudong Liu[1], Biao Zhang[1], Christos Tachtatzis[4], Chuanlong Xu[1*]

[1] Key Laboratory of Energy Thermal Conversion and Control of Ministry of Education, School of Energy and Environment, Southeast University, Nanjing 210096, PR China

[2] School of Engineering and Digital Arts, University of Kent, Canterbury, Kent, CT2 7NT, UK

[3] Sunny Central Research Institute, No. 1190, Bin'an Road, Binjiang District, Hangzhou 310052, PR China

4 Department of Electronic and Electrical Engineering, University of Strathclyde, Glasgow, G1 1XW, UK

E-mails:
eelijian@seu.edu.cn
M.Hossain@kent.ac.uk
sunjun@sunnyoptical.com
yudong.liu@seu.edu.cn
zhangbiao@seu.edu.cn
christos.tachtatzis@strath.ac.uk
chuanlongxu@seu.edu.cn*

*Corresponding author: Tel: +86 025 83794395

Abstract

It is important to identify boundary constraints in the inverse algorithm for the reconstruction of flame temperature because a negative temperature can be reconstructed with improper boundary constraints. In this study, a hybrid algorithm, a combination of Levenberg-Marquardt with boundary constraint (LMBC) and non-negative least squares (NNLS), was proposed to reconstruct the flame temperature and absorption coefficient simultaneously by sampling the multi-wavelength flame radiation with a colored plenoptic camera. To validate the proposed algorithm, numerical simulations were carried out for both the symmetric and asymmetric distributions of the flame temperature and absorption coefficient. The plenoptic flame images were modeled to investigate the characteristics of flame radiation sampling. Different Gaussian noises were added into the radiation samplings to investigate the noise effects on the reconstruction accuracy. Simulation results showed that the relative errors of the reconstructed temperature and absorption coefficient are less than 10%, indicating that accurate and reliable reconstruction can be obtained by the proposed algorithm. The algorithm was further verified by experimental studies, where the reconstructed results were compared with the thermocouple measurements. The simulation and experimental results demonstrated that the proposed algorithm is effective for the simultaneous reconstruction of the flame temperature and absorption coefficient.

Keywords— 3-D reconstruction; Flame temperature; Absorption coefficient; Plenoptic imaging;

Levenberg-Marquardt with boundary constraint; Non-negative least squares

1. Introduction

The haze caused by combustion emissions like particulate matter (PM) has become a serious environmental problem in China. A large amount of smoke, dust and nitrogen oxide (NO_X) is emitted from coal and natural gas combustion furnaces [1, 2]. It is significant and urgent to investigate the combustion process which emits harmful products into the atmosphere. The temperature is a vital factor that affects the generation of combustion emissions including PMs and NOx. Therefore, in order to control and improve the combustion process, it is necessary to measure the flame temperature accurately and thus precise measurement techniques are required. Many studies have been devoted to the area of the flame temperature measurements [3-17], including one-dimensional (1-D) [10, 11], two-dimensional (2-D) [9, 12-14] and three-dimensional (3-D) [3, 15-17] technologies. In general, the 1-D or 2-D methods can only provide the temperature information in a limited region of the flame, such as the temperature of single volume [11] or the 2-D temperature distributions over a light sheet [12]. However, the flame is a precipitating medium with three spatial dimensions in nature. Therefore, it is desirable to measure the 3-D flame temperature field, which can provide an in-depth understanding of flame. To achieve this, advanced and precise 3-D measurement techniques are necessarily required for the flame temperature measurement.

In general, there are two kinds of technologies for the investigation of 3-D flame temperature field [5, 8, 18-25]. One is the laser-based method, which utilizes the spectral response to the imposed external laser light to calculate the flame temperature [8, 16, 21]. Another approach, known as an image-based method, incorporates conventional CCD or CMOS cameras and 3-D techniques to sample the flame self-radiation and then reconstruct the temperature distribution [4, 20, 22-24]. For both methods, multiple cameras or optical sensing arrangements [17] are required to obtain the flame radiation information in multiple directions for the 3-D temperature reconstruction. However, for the image-based method, no external laser light is required and thus it is simple in equipment, low cost, easy to install, more suitable and potential for the large-scale application in the hostile industrial environments such as coal/biomass-fired furnace [24].

Various techniques based on the image-based method have been developed to reconstruct the 3-D flame temperature profile [4, 19, 25]. Gong et al. [19] proposed a combination of optical sectioning tomography (OST) and two-colour method to reconstruct the temperature of impinging flames. However, the flame radiation captured by the photosensor depends on both the flame temperature and radiative properties. The absorption and scattering effects of the flame on the radiative transfer were not considered in their measurement technique and thus the reconstructed temperature may not accord with the realistic radiation transfer inside the flame [26, 27]. Inversed radiative transfer (IRT) method also can be used to calculate the temperature of each flame voxel by solving the radiative transfer model with suitable inverse reconstruction algorithms [22, 28-30]. But, it is still crucial to know beforehand the flame radiative properties for the temperature measurement. Although the empirical value of the flame radiative properties could be used to reconstruct the flame radiation intensity with the IRT method, the reconstruction accuracy is limited due to the inaccurately assumed radiative properties [7, 31]. A better choice for solving this issue is to estimate the 3-D flame temperature distribution and radiative properties simultaneously by using inverse algorithms such as LSQR-PSO [32, 33]. However, negative values can be obtained during solving the radiation intensity and properties, and boundary constraints to deal with the negative values have not been investigated [5, 32, 33]. Noted that the inverse problem of flame radiation is normally ill-posed and its solutions are mathematically ambiguous, negative solutions may occur during the required iterations and thus render inaccurate flame temperature reconstruction. Consequently, boundary constraint must be considered for solving inverse radiation problems accurately.

To reduce the number of cameras required for the image-based method, a single plenoptic camera with microlens array mounted above the photosensor was utilized for the flame temperature measurement [5, 7, 34]. It is capable of sampling the 3-D flame radiation and reconstructing the 3-D flame temperature because the direction and position of each radiation sample can be traced with the benefits of the microlens array [7]. Huang et al. [5] developed a hybrid LSQR–CG (Conjugated Gradient) algorithm based on multi-spectral light-field imaging technique. Li et al. [34] simplified the reconstruction process by simulating the plenoptic imaging of the temperature distribution by a plenoptic camera model based on the Monte Carlo method. Although the IRT methods based on the

plenoptic camera were verified for the flame temperature reconstruction, the boundary constraint has not been investigated, especially for the non-negativity of the reconstruction results. Moreover, simple setting the negative values of boundary constraint to be zero obtained during each iteration may cause divergence. Thus, further practical applications are limited for the temperature reconstruction of realistic flames.

In this study, a hybrid LMBC-NNLS algorithm with non-negative boundary constraint is proposed and discussed in details to reconstruct the flame temperature and absorption coefficient simultaneously. A radiative model based on the plenoptic imaging technique is developed to retrieve the multi-wavelength flame radiation sampling. Numerical simulations were performed to validate the proposed hybrid algorithm, where different distributions of flame temperature and absorption coefficient were considered to evaluate the robustness and accuracy of the hybrid algorithm. Experimental studies were also carried out to reconstruct the flame temperature and absorption coefficient under different combustion conditions. The reconstructed results were compared with the thermocouple measurements and discussed.

2. Measurement principle

2.1 Multi-wavelength flame radiation sampling

The sooty flame can emit thermal radiation including visible wavelengths towards the surroundings [35]. The flame radiation at the visible wavelengths can be sampled by a colored plenoptic camera with an optical filter array. Basically, the filter array consists of many filters and each pixel of the light field sensors is covered by a single filter to detect the flame radiation at the visible wavelengths, i.e., red (R), green (G) and blue (B). Reversely, the flame temperature and absorption coefficient can be retrieved through the sampled radiation intensity. In this work, the R and G channels were chosen for the flame temperature and absorption coefficient reconstruction because they have higher spectral sensitivities on CCD sensor than the B channel, giving a better signal-to-noise ratio.

Fig. 1 illustrates the schematic of the multi-wavelength flame radiation sampling through the colored plenoptic camera. Here, the RGB Bayer pattern is selected as a filter array due to its wide usage. a, m and p denote the planes of the main lens, microlens array and photosensor, respectively. The intermediate plane i is the conjugate plane of plane p relative to the microlens array. The virtual object plane v is the conjugate plane of plane i relative to the main lens. The flame radiation along a detection path is detected by a pixel on the photosensor of the plenoptic camera with the direction and starting position at plane o. The red or green lines denote the detection path of each pixel. $\boldsymbol{F}$ is the direction angle vector of the detection path (polar angle θ_o and azimuthal angle ψ_o) and $\boldsymbol{W}$ is the coordinate vector (x_s, y_s, z_s) of the starting point at plane o.

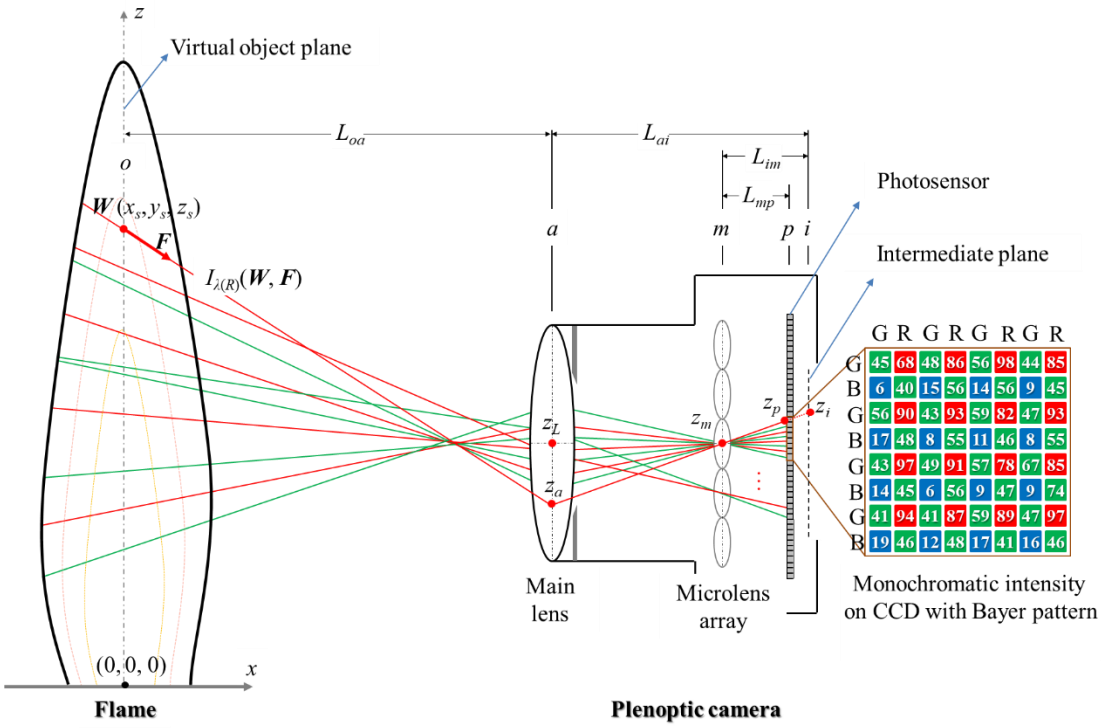

Fig. 1. Schematic of the multi-wavelength flame radiation sampling through the colored plenoptic camera.

In order to calculate $\boldsymbol{F}$ and $\boldsymbol{W}$, the Cartesian coordinate system is set on the flame central point of the bottom part (considered as a flat surface). The x-axis is parallel to the optical axis of the camera and the y-axis belongs to the bottom part of the flame. In this coordinate system, $x_s = 0$ and only y_s and z_s coordinates are required to calculate. $\boldsymbol{F}$ and $\boldsymbol{W}$ are then obtained by calculating the intersection point between the ray detection path and each plane. The detailed procedure is described as follows:

Step 1. The sampled radiation from each pixel passes through the pixel Z_p, the center of the corresponding microlens Z_m, the corresponding points Z_i and Z_a at plane i and plane a (refer to Fig. 1). Its intensity is denoted as $I_\lambda(\boldsymbol{W}, \boldsymbol{F})$ with a unit of $W/(m^3 \cdot sr)$. According to the intercept theorem [36], the coordinates $Z_a(y_a, z_a)$ and $Z_i(y_i, z_i)$ can be calculated by the following equations:

$$\begin{bmatrix} y_a \\ z_a \end{bmatrix} = \begin{bmatrix} 1+\dfrac{L_{am}}{L_{mp}} & 0 \\ 0 & 1+\dfrac{L_{am}}{L_{mp}} \end{bmatrix} \begin{bmatrix} y_m \\ z_m \end{bmatrix} + \begin{bmatrix} -\dfrac{L_{am}}{L_{mp}} & 0 \\ 0 & -\dfrac{L_{am}}{L_{mp}} \end{bmatrix} \begin{bmatrix} y_p \\ z_p \end{bmatrix} \tag{1}$$

$$\begin{bmatrix} y_i \\ z_i \end{bmatrix} = \begin{bmatrix} 1+\dfrac{L_{im}}{L_{mp}} & 0 \\ 0 & 1+\dfrac{L_{im}}{L_{mp}} \end{bmatrix} \begin{bmatrix} y_m \\ z_m \end{bmatrix} + \begin{bmatrix} -\dfrac{L_{im}}{L_{mp}} & 0 \\ 0 & -\dfrac{L_{im}}{L_{mp}} \end{bmatrix} \begin{bmatrix} y_p \\ z_p \end{bmatrix} \tag{2}$$

where (y_m, z_m) and (y_p, z_p) are the center coordinates of the corresponding microlens and pixel, respectively. L_{am} is the separation from the plane a to plane m. L_{im} is the separation from plane i to plane m. L_{mp} is the separation from plane m to plane p.

Step 2. The points at planes o and i are conjugated to the main lens and they are in one line. Based on the intercept theorem [36], the coordinate of the corresponding point at plane o can be calculated by

$$\begin{aligned}\begin{bmatrix} y_s \\ z_s \end{bmatrix} &= \begin{bmatrix} 1+\dfrac{L_{oa}}{L_{am}} & 0 \\ 0 & 1+\dfrac{L_{oa}}{L_{am}} \end{bmatrix}\begin{bmatrix} y_L \\ z_L \end{bmatrix} + \begin{bmatrix} -\dfrac{L_{oa}}{L_{ai}} & 0 \\ 0 & -\dfrac{L_{oa}}{L_{ai}} \end{bmatrix}\begin{bmatrix} y_i \\ z_i \end{bmatrix} \\ &= \begin{bmatrix} 1+\dfrac{L_{oa}}{L_{am}} & 0 \\ 0 & 1+\dfrac{L_{oa}}{L_{am}} \end{bmatrix}\begin{bmatrix} y_L \\ z_L \end{bmatrix} + \begin{bmatrix} -\dfrac{L_{oa}}{L_{ai}}\left(1+\dfrac{L_{im}}{L_{mp}}\right) & 0 \\ 0 & -\dfrac{L_{oa}}{L_{ai}}\left(1+\dfrac{L_{im}}{L_{mp}}\right) \end{bmatrix}\begin{bmatrix} y_m \\ z_m \end{bmatrix} \\ &\quad + \begin{bmatrix} \dfrac{L_{oa}L_{im}}{L_{ai}L_{mp}} & 0 \\ 0 & \dfrac{L_{oa}L_{im}}{L_{ai}L_{mp}} \end{bmatrix}\begin{bmatrix} y_p \\ z_p \end{bmatrix}\end{aligned} \tag{3}$$

where (y_L, z_L) is the optical center coordinate of the main lens. L_{oa} is the separation from plane o to plane a and L_{ai} is the separation from the plane a to plane i.

Step 3. According to the known coordinates of the points at the planes o and a, the direction $\boldsymbol{F}$ (θ_o, ψ_o) of the flame radiation is obtained by

$$\begin{aligned}\theta_o &= \arccos\left[\frac{(z_a - z_s)}{\sqrt{(x_a - x_s)^2 + (y_a - y_s)^2 + (z_a - z_s)^2}}\right] \\ &= \arccos\left[\frac{(z_a - z_s)}{\sqrt{L_{oa}{}^2 + (y_a - y_s)^2 + (z_a - z_s)^2}}\right]\end{aligned} \tag{4}$$

$$\psi_o = \begin{cases} \arctan\left(\dfrac{y_a - y_s}{x_a - x_s}\right) = \arctan\left(\dfrac{y_a - y_s}{L_{oa}}\right) & y_a \geq y_s \\ \arctan\left(\dfrac{y_a - y_s}{x_a - x_s}\right) + 2\pi = \arctan\left(\dfrac{y_a - y_s}{L_{oa}}\right) + 2\pi & y_a < y_s \end{cases} \tag{5}$$

Once $\boldsymbol{F}$ and $\boldsymbol{W}$ are determined, the flame radiation intensity can be obtained by solving the following radiative transfer equation [33]:

$$\frac{\mathrm{d}\, I_\lambda(\boldsymbol{W}, \boldsymbol{F})}{\mathrm{d}\, a} = K \cdot I_{b\lambda}(\boldsymbol{W}) - \beta \cdot I_\lambda(\boldsymbol{W}, \boldsymbol{F}) + \frac{\sigma}{4\pi}\int_{4\pi} I_\lambda \Phi(\boldsymbol{F}', \boldsymbol{F})\, \mathrm{d}\, \Omega \tag{6}$$

where $I_{b\lambda}$ is the blackbody radiation intensity at position $\boldsymbol{W}$ at a wavelength of λ, $W/(m^3 \cdot sr)$. $\Phi(\boldsymbol{F}', \boldsymbol{F})$ is the scattering phase function between the incident direction $\boldsymbol{F}'$ and the scattering direction $\boldsymbol{F}$. a is the length of the ray direction $\boldsymbol{F}$. Ω is the solid angle in direction $\boldsymbol{F}'$. K, β and σ are the absorption, emission and scattering coefficients, respectively. The relationship between $I_{b\lambda}$ and temperature T can be expressed by

$$T = c_2 / \lambda \ln[c_1 / (\lambda^5 \pi I_{b\lambda}) + 1] \tag{7}$$

where c_1 is the first radiation constant, 3.7418×10^{-16} W·m^2 and c_2 is the second radiation constant,

1.4388×10^{-2} m·K.

On a monochromatic basis, the spectral emissivity of a luminous flame can be calculated by [37]:

$$\varepsilon_\lambda = 1-\exp\left[-\left(K_{\omega\lambda}X_\omega + K_{c\lambda}X_c + K_{s\lambda}X_s\right)\right] \tag{8}$$

where $K_{\omega\lambda}$, $K_{c\lambda}$ and $K_{s\lambda}$ are the spectral absorption coefficients of the water vapor, carbon dioxide and soot, respectively. X_ω and X_c are the mass path lengths for the water vapor and carbon dioxide. X_s is the geometric length of flame. The scattering contribution of the soot particles within flame is neglected because the soot particles are both absorptive and small (less than 0.1 μm). The calculation results of the Mie theory also verified that the scattering cross-section is much smaller than the absorption cross-section. In this study, the scattering process of the participating media is ignored and only the absorption is taken into consideration. The radiation intensity of the flame $I_\lambda(\boldsymbol{W}, \boldsymbol{F})$ along the detection path ($\boldsymbol{W}$, $\boldsymbol{F}$) is then obtained by solving Eq. (6) through the discretized solution:

$$I_\lambda\left(\boldsymbol{W},\boldsymbol{F}\right) = I_{b\lambda}^n\left[1-\exp(-a_nK_n)\right] + \sum_{i=1}^{n-1}\left[\exp\left(-\sum_{j=i+1}^{n}a_jK_j\right) - \exp\left(-\sum_{j=i}^{n}a_jK_j\right)\right]I_{b\lambda}^i \tag{9}$$

where n is the total number of voxels the flame radiation passes through. i and j are the i^{th} and j^{th} voxels along the flame detection path ($\boldsymbol{W}$, $\boldsymbol{F}$), respectively. According to Eqs. (6)-(9), the radiation intensity $I_\lambda(\boldsymbol{W}, \boldsymbol{F})$ emitted by the flame depends on the flame temperature and the absorption coefficient along the detection path ($\boldsymbol{W}$, $\boldsymbol{F}$).

2.2 Hybrid LMBC-NNLS inversion algorithm

From the sampled flame radiation by the plenoptic camera, a linear system is derived based on the radiative equation (9) and defined as follows:

$$\begin{bmatrix} I_\lambda^1 \\ I_\lambda^2 \\ \vdots \\ I_\lambda^m \end{bmatrix} = \begin{bmatrix} A_1^1 & A_2^1 & \cdots & A_n^1 \\ A_1^2 & A_2^2 & \cdots & A_n^2 \\ \vdots & \vdots & \ddots & \vdots \\ A_1^m & A_2^m & \cdots & A_n^m \end{bmatrix}\begin{bmatrix} I_{b\lambda}^1 \\ I_{b\lambda}^2 \\ \vdots \\ I_{b\lambda}^n \end{bmatrix} \tag{10}$$

$$\begin{cases} A_i^j = \exp(-\sum_{J=I_i^j+1}^{N^j}a_JK_J) - \exp(-\sum_{J=I_i^j}^{N^j}a_JK_J) & I_i^j < N^j \\ A_i^j = 1-\exp(-\sum_{J=I_i^j}^{N^j}a_JK_J) & I_i^j = N^j \end{cases} \tag{11}$$

$$\boldsymbol{I}_\lambda = \boldsymbol{A}\,\boldsymbol{I}_{b\lambda} \tag{12}$$

where $\boldsymbol{I}_\lambda$ is the flame radiation intensity vectors; $\boldsymbol{I}_{b\lambda}$ is the blackbody radiation intensity vectors. $\boldsymbol{A}$ is the coefficient matrix and calculated by Eq. (11). m and n are the total numbers of detected paths and flame voxels, respectively. i and j are the i^{th} detected path and j^{th} flame voxel, respectively. N_j is the number of flame voxels passed through the j^{th} detected path. I and J are the I^{th} and J^{th} voxels of flame along the j^{th} detected path, respectively.

It is required to solve Eq. (12) for the flame temperature reconstruction. However, the absorption coefficient and the temperature are both unknown for the realistic flames (refer to Section 4). To solve this issue, a hybrid algorithm combining non-negative least squares(NNLS) and Levenberg–Marquardt with Boundary Constraint (LMBC) is proposed to solve Eq. (12) for the simultaneous reconstruction of flame temperature and absorption coefficient. NNLS is firstly used to solve linear least square problems through the computation of the pseudo-inverse. Compared to other linear algorithms such as LSQR and Truncated Singular Value Decomposition (TSVD), the non-negativity of the reconstruction results by NNLS can be guaranteed. But, it is still unable to solve Eq. (12)

independently because the unknown temperature distribution and the absorption coefficient of flame make the Eq. (12) nonlinear. In this study, a nonlinear optimization method, i.e., Levenberg–Marquardt (LM) algorithm, is therefore combined to solve this problem [39, 40]. The LM algorithm can add non-negative constraints to the solutions of Eq. (10) in the process of flame temperature reconstruction. It is generally used for solving nonlinear least squares problems to obtain $\boldsymbol{A}$ when $\boldsymbol{I}_{b\lambda}$ and $\boldsymbol{I}_{\lambda}$ are known. It also has better performance of global convergence and non-dependence of initialization than other nonlinear algorithms such as Conjugate Gradient (CG). More importantly, boundary constraints can be easily considered in the LM algorithm without iteration convergence. The LM algorithm with boundary constraints projecting estimated parameter onto the range of $[l, u]$ in each iteration is named by LMBC in this study [41]. More details can be found in Step 6 in the following LMBC-NNLS procedures. In LMBC, the upper boundary u and lower boundary l are determined by the specific inverse problem. During the flame temperature reconstruction, the lower boundary l is normally set to zero due to the impossibility of negative absorption coefficient. The upper boundary u depends on the flame combustion characteristics. For instance, due to the limited absorbing ability of particles and gas molecule inside the ethylene diffusion flame utilized in this study (Section 4.1), the absorption coefficient couldn't be too high and therefore u is set to 1000.

In the hybrid LMBC-NNLS algorithm, the objective function is applied to optimize the temperature and absorption coefficient as follows:

$$F\left(\boldsymbol{T},\boldsymbol{K}\right)=\left\|\boldsymbol{I}'_{\lambda(G)}-\boldsymbol{I}_{\lambda(G)}\right\| \tag{13}$$

where $\boldsymbol{I}_{\lambda(\mathrm{G})}$ and $\boldsymbol{I}'_{\lambda(\mathrm{G})}$ are measured and assumed radiation intensity vectors, respectively. Fig. 2 shows the implementation procedures of the hybrid LMBC-NNLS algorithm and they are described in detail as follows:

Step 1. Set the initial values such as number of iterations $k = 0$ and $k_{\max} = 200$, intermediate parameters $v = 2$ and $\eta = 2$, vector of absorption coefficient $\boldsymbol{K} = \boldsymbol{K}_0 = 1$ (unit vector). Calculate the symmetric matrix $\boldsymbol{\Omega}$, the difference between the measured and the assumed intensity $\boldsymbol{r}$, gradient of the objective function $\boldsymbol{g}$, index to stop the iteration S_{tp} and the damping factor μ by the following equations (14) – (18).

$$\boldsymbol{\Omega}=\boldsymbol{J}^{T}\boldsymbol{J} \tag{14}$$

$$\boldsymbol{r}=\boldsymbol{I}'_{\lambda(G)}-\boldsymbol{I}_{\lambda(G)} \tag{15}$$

$$\boldsymbol{g}=\boldsymbol{J}^{T}\boldsymbol{r} \tag{16}$$

$$S_{tp}=\left(\left\|\boldsymbol{g}\right\|\le\varepsilon_1\right) \tag{17}$$

$$\mu=\eta\cdot\max_{i=1,\ldots,m}(\Omega_{ii}) \tag{18}$$

where $\boldsymbol{J}$ is the Jacobian matrix of the first-order partial derivatives of the function $\boldsymbol{I}'_{\lambda(\mathrm{G})}$ for variable $\boldsymbol{K}$. ε_1 is a threshold and set to 1×10^{-10}. Ω_{ii} is the diagonal elements of the matrix $\boldsymbol{\Omega}$.

Step 2. Determine the coefficient $\boldsymbol{A}$ based on Eq. (11) for variable $\boldsymbol{K}$ and then solve Eq. (12) using the NNLS algorithm with the calculated coefficient $\boldsymbol{A}$ and the intensity $\boldsymbol{I}_{\lambda(\mathrm{R})}$ captured by the plenoptic camera. Then calculate the radiative blackbody intensity $I_{b\lambda}$ of each flame voxel.

Step 3. The flame temperature T of each voxel is calculated by Eq. (7) with the obtained blackbody radiation intensity $I_{b\lambda}$.

Step 4. The blackbody radiation intensity $I_{b\lambda}$ of each voxel is determined by rearranging Eq. (7)

with temperature $\boldsymbol{T}$. The function $\boldsymbol{I}'_{\lambda(\mathrm{G})}$ is determined according to Eq. (11) with absorption coefficient $\boldsymbol{A}$ and the monochromatic intensity of blackbody $I_{b\lambda}$.

Step 5. Calculate the Jacobian matrix $\boldsymbol{J}$ of the function $\boldsymbol{I}'_{\lambda(\mathrm{G})}$ for $\boldsymbol{K}$ and determine $\boldsymbol{\Omega}$, $\boldsymbol{r}$ and $\boldsymbol{g}$ using Eqs. (14)-(16). The LM step of $\boldsymbol{\Delta}$ is obtained by Eq. (19) and checked with a threshold value of 1e-10.

$$\left(\boldsymbol{\Omega}+\mu\boldsymbol{I}\right)\boldsymbol{\Delta}=\boldsymbol{g} \tag{19}$$

where $\boldsymbol{I}$ is the unit matrix.

Step 6. The absorption coefficients $\boldsymbol{K}_{\mathrm{new}}$ is obtained for the optimization step $\boldsymbol{\Delta}$ and projected onto the constraint set Q according to the following equations:

$$P_Q\left(\boldsymbol{K}\right)=\max\left\{\min\left\{\boldsymbol{K},\boldsymbol{u}\right\},\boldsymbol{l}\right\} \tag{20}$$

$$Q=\left\{\boldsymbol{K}\in\mathbf{R}^m \mid l_i\le K_i\le u_i, i=1,\ldots,m\right\} \tag{21}$$

where $\boldsymbol{l}$ ($[l_1, l_2, \ldots, l_{\mathrm{m}}]$) and $\boldsymbol{u}$ ($[u_1, u_2, \ldots, u_{\mathrm{m}}]$) are the lower and upper boundaries of the absorption coefficient. The values of the absorption coefficient are then constrained to the range of $[\boldsymbol{l}, \boldsymbol{u}]$.

Step 7. The iteration index ρ is determined by Eq. (21) and the decreasing of the iteration index ρ can indicate the converging of the reconstruction.

$$\rho=\frac{\left\|\boldsymbol{r}\right\|^2-\left\|\boldsymbol{I}_{\lambda(G)}-\boldsymbol{I}'_{\lambda(G)}\right\|^2}{\boldsymbol{\Delta}\left(\mu\boldsymbol{\Delta}+\boldsymbol{g}\right)} \tag{22}$$

Step 8. Update $\boldsymbol{K}$ with the $\boldsymbol{K}_{\mathrm{new}}$ and calculate $\boldsymbol{\Omega}$, $\boldsymbol{r}$ and $\boldsymbol{g}$ according to Eqs. (14) - (16). The S_{tp} and μ are calculated by the following two equations. Also, check the S_{tp} to see whether the iterations can be stopped or not.

$$S_{tp}=\left(\left\|\boldsymbol{g}\right\|_\infty\le\varepsilon_1\right)\mathrm{or}\left(\left\|\boldsymbol{r}\right\|\le\varepsilon_1\right) \tag{23}$$

$$\mu=\mu\cdot\max\left[1/3,1-\left(2\rho-1\right)^3\right] \tag{24}$$

Step 9. Finally, the optimal solution of flame temperature $\boldsymbol{T}$ and absorption coefficient $\boldsymbol{K}$ are obtained by multi-iterations.

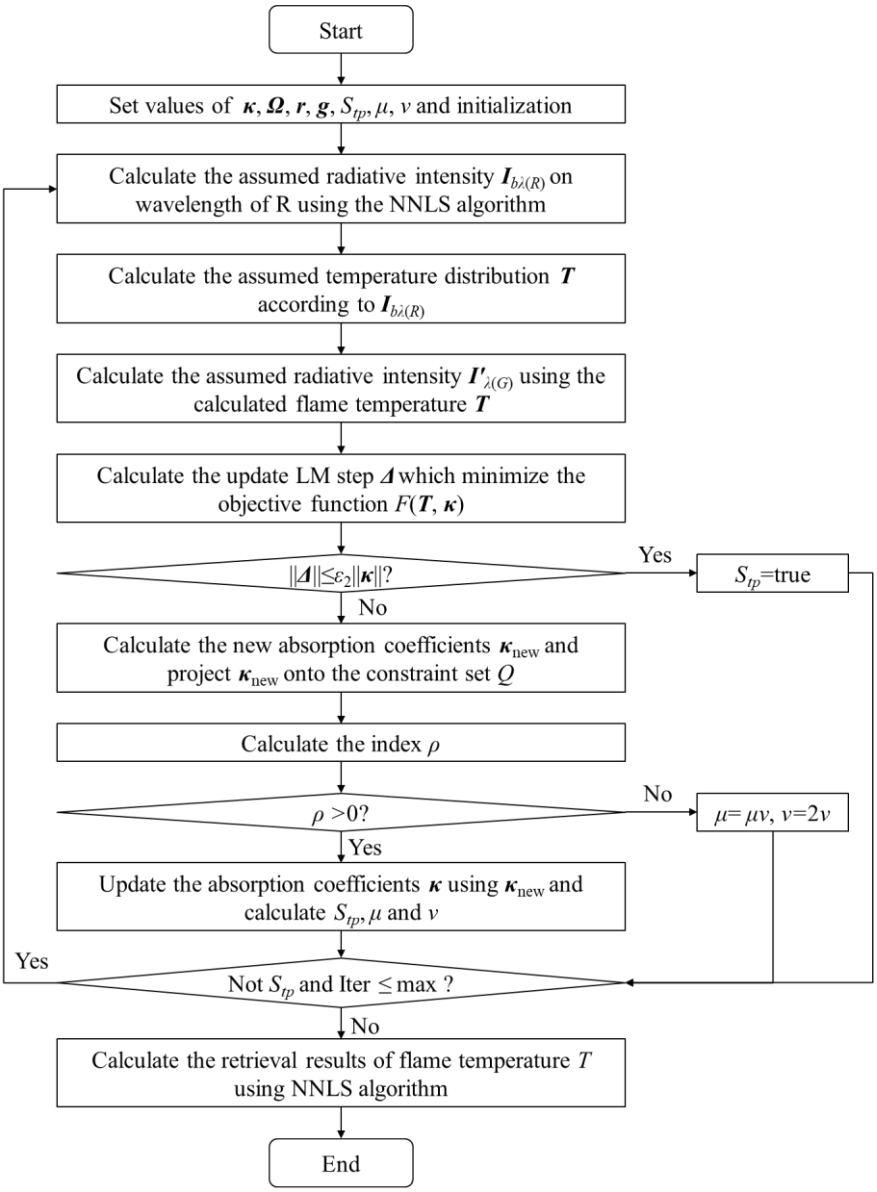

Fig. 2. The flowchart of the hybrid LMBC-NNLS algorithm.

3. Numerical Simulations

3.1 Simulation setup

In this study, numerical simulations were carried out to validate the proposed LMBC-NNLS algorithm. A cylindrical flame is considered in the simulation to reconstruct the temperature and absorption coefficient. The radius (*R)* and the height (*Z)* of the simulated cylindrical flame were respectively set to 8 mm and 30 mm because the radius of experimental flame is about 8 mm and the height varies from 14 - 44 mm, as described in Section 3.2. Two cases were considered in the simulation to investigate the reconstruction accuracy under different combustion conditions. The distributions of temperature and absorption coefficient are considered as symmetrical in Case 1 (T_1, K_1) and asymmetrical in Case 2 (T_2, K_2). The symmetrical distribution along the *z*-axis was set based on Ref. [6] for ethylene flames while the asymmetrical distribution along the *z*-axis was based on the Ref. [33]. For both cases, the temperature range was set to be 900 - 2100 K and the absorption coefficients K_1 and K_2 were set to be 0- 30 m^{-1} for the ethylene flame [42]. T_1, K_1, T_2 and K_2 are expressed in Eqs. (25- 28) and plotted in Fig. 3.

$$T_1(r,z)=1200\exp\left\{-\left[3\left(\frac{r^2}{R^2}+\frac{z^2}{Z^2}\right)-0.9\right]^2\right\}+900 \tag{25}$$

$$K_1(r,z)=30\exp\left\{-100\left[\left(\frac{r^2}{R^2}+\frac{z^2}{Z^2}\right)-0.6\right]^2\right\}+5 \tag{26}$$

$$T_2(x,y,z)=\frac{2200}{3}\left\{\begin{array}{l}\exp\left\{\begin{array}{l}-40\left[(750x+7.5)/9-1.1\right]^2\\-25\left[(750y+8.5)/9-0.8\right]^2\end{array}\right\}\\+0.8\exp\left\{\begin{array}{l}-25\left[(750x+7.5)/9-0.8\right]^2\\-35\left[(750y+8.5)/9-1.2\right]^2\end{array}\right\}\end{array}\right\}+880(1-100z/3)+753 \tag{27}$$

$$K_2(x,y,z)=\frac{50}{3}\left\{\begin{array}{l}\exp\left\{\begin{array}{l}-40\left[(750x+7.5)/9-1.1\right]^2\\-25\left[(750y+8.5)/9-0.8\right]^2\end{array}\right\}\\+0.8\exp\left\{\begin{array}{l}-25\left[(750x+7.5)/9-0.8\right]^2\\-35\left[(750y+8.5)/9-1.2\right]^2\end{array}\right\}\end{array}\right\}+20(1-100z/3)+5/3 \tag{28}$$

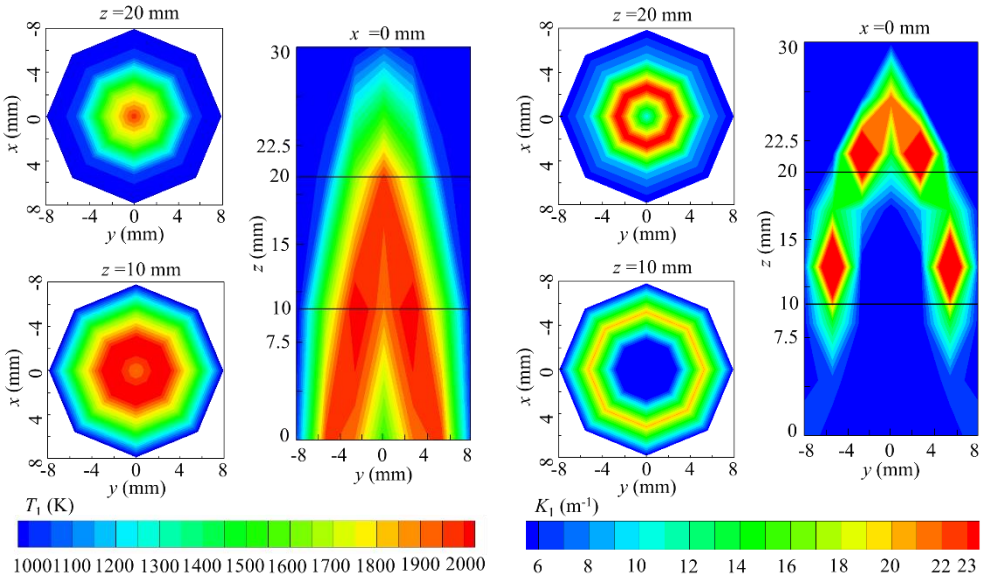

(a) Case 1

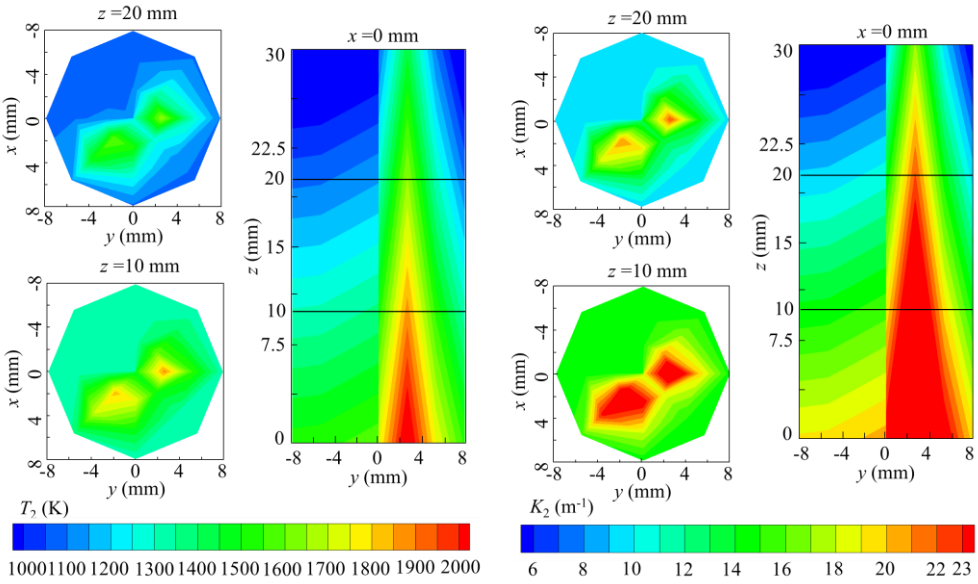

(b) Case 2

Fig. 3. Distributions of T_1, K_1, T_2 and K_2.

The parameters of the focused plenoptic camera were shown in Table 1. Here, f and f_m are the focal lengths of the main lens and the microlens array, respectively. N_m is the number of microlens along the horizontal/vertical direction of the microlens array. N_p is the number of pixels covered by each microlens array along the horizontal/vertical direction. d_p is the length of each pixel and d_m is the diameter of each microlens.

Table 1. Parameters of the focused plenoptic camera

L_{oa} (mm)	L_{ai} (mm)	L_{im} (mm)	L_{mp} (μm)	F (mm)	f_m (μm)	N_m	N_p	d_p (μm)	d_m (μm)
505	55.5	2.4	480	50	600	60	12	8	95

In order to obtain the flame radiation intensity $I_{\lambda(R)}$ and $I_{\lambda(G)}$, the whole flame was discretized into 64 ($4 \times 4 \times 4$) voxels in the circumferential (C_r), axial (Z_r) and radial (R_r) directions. Fig. 4 illustrates the division and voxels of the cylindrical flame where the i^{th} flame voxel is numbered according to the division in C_r, Z_r and R_r directions. The position and direction of the flame radiation were calculated with Eqs. (3) - (5). $I_{\lambda(R)}$ and $I_{\lambda(G)}$ were then calculated according to Eq (12). To obtain plenoptic images of the flame, the intensity of $I_{\lambda(R)}$ and $I_{\lambda(G)}$ were linearly mapped to a gray level in the range of 0- 255, as shown in Fig. 5. It was observed that the brightness of the simulated flames mainly depends on the temperature distribution over the longitude-sections (y-z plane) (Fig. 3). Although the distribution of the absorption coefficient can also be affected by the flame brightness, the temperature is the dominant factor for the brightness level of the flame light field image. Therefore, the radiation intensity of each pixel is more sensitive to the temperature, rather than the absorption coefficient.

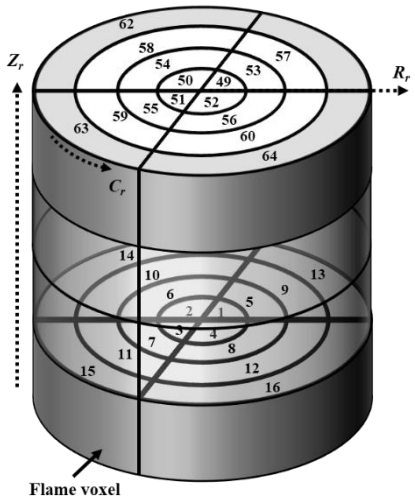

Fig. 4. Example of divisions and voxels of the cylindrical flame.

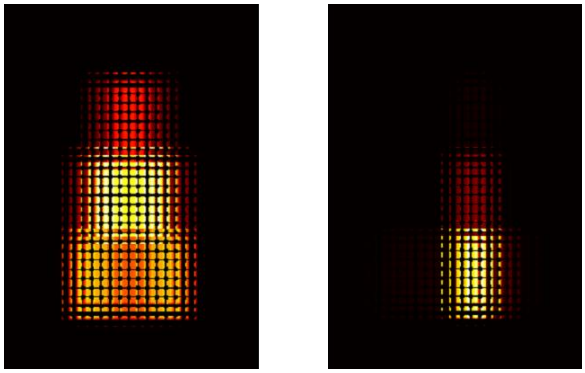

(a) Symmetric (Case 1) (b) Asymmetrical (Case 2)

Fig. 5. Simulated plenoptic flame images for Case 1 and Case 2.

3.2 Performance validation

To investigate the performance of the proposed algorithm for different signal-to-noise ratios (*SNRs*, defined in Eq. (29)), 20, 30 and 40 dB Gaussian noises were added into the radiation intensity $I_{\lambda(\mathrm{R})}$ and $I_{\lambda(\mathrm{G})}$. The temperature and the absorption coefficient were then reconstructed using the proposed LMBC-NNLS algorithm.

$$SNR = 10\log_{10}\left[\frac{\sum_{i=1}^{k}\left(I_{\lambda}^{i}\right)^{2}}{\sum_{i=1}^{k}\left(N_{i}\right)^{2}}\right] \tag{29}$$

Firstly, to investigate the non-negativity of the inverse problem by the proposed algorithm for solving the flame temperature, the LMBC-NNLS is compared with LMBC-LSQR (without boundary constraint) [5]. The $I_{\lambda(\mathrm{R})}$ is compared when *SNR* = 20 dB for Case 2. The procedures of LMBC-LSQR are similar to LMBC-NNLS, by replacing NNLS with LSQR in **Step 2** in Section 2.2. Fig. 6 shows the reconstructed results by LMBC-NNLS and LMBC-LSQR. Noted that negative radiation intensity values were obtained at the first iteration for LMBC-LSQR, the temperature cannot be calculated using these negative values and therefore the iteration stopped at the first iteration. Thus, only reconstructed values at the first iteration are presented in Fig. 6 (a). It also can be seen that 19 negative intensity values were generated in the reconstructed results by the LMBC-LSQR algorithm. Even though some zero values are observed at the first iteration for LMBC-NNLS,

the flame temperature can be calculated in **Step 2** and the iterations can still continue to the final convergence. For the final converged results of LMBC-NNLS, the inaccuracy caused by zero values can be compensated through interpolation methods. Particularly, the zero intensity of each flame voxel generated by NNLS at the final convergence can be interpolated by averaging non-zero values of flame voxels in the spatial neighbourhood. No negative values were then obtained by the proposed LMBC-NNLS.

The LMBC-NNLS is also compared with LM (without boundary constraint)-NNLS to investigate the non-negativity of the proposed algorithm for solving the absorption coefficient. The comparison is also carried out when *SNR* = 20 dB in Case 2. The procedures of LM-LSQR are Similar to LMBC-NNLS except for **Step 6** in Section 2.2. The reconstructed absorption coefficient of the flame voxels at the final convergence is shown in Fig. 6 (b). For the LM-NNLS, the negative value (refer to the 8th flame voxel) of the absorption coefficient can be seen in the reconstructed results. For the 7th flame voxel, a great difference can be observed between the reconstructed absorption coefficient and the set value. For the LMBC-NNLS, non-negative values were obtained and a much smaller difference can be seen between the reconstructed absorption coefficient and the set value. Generally, the LMBC-NNLS improves the accuracy of the simultaneous reconstruction of flame temperature and absorption coefficient.

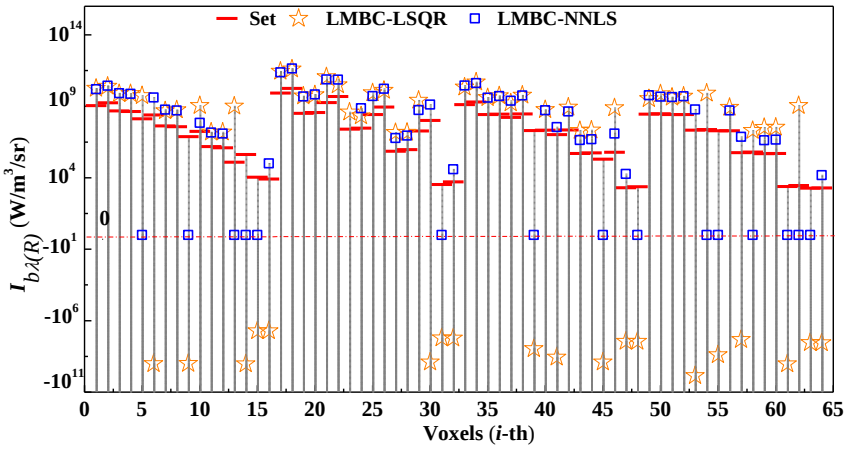

(a) Distribution of radiation intensity

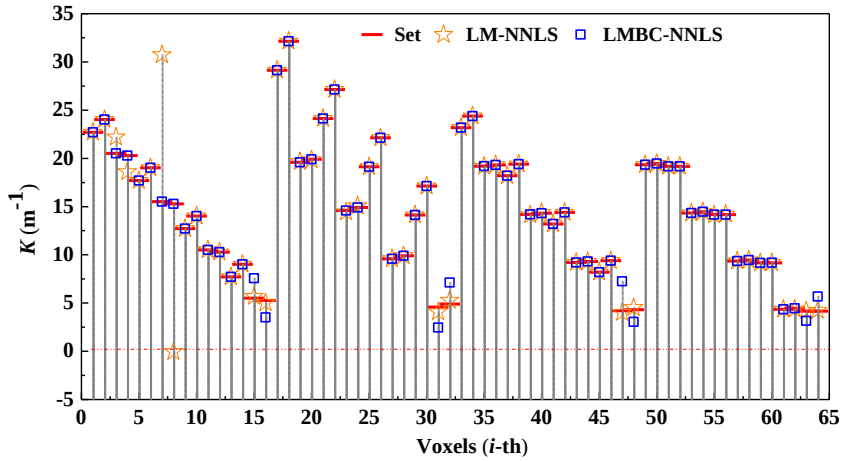

(b) Distribution of the absorption coefficient

Fig. 6. Reconstructed radiation intensity and absorption coefficient for different algorithms.

3.3 Reconstruction of simulated flame temperature and absorption coefficient

The LMBC-NNLS algorithm is applied to reconstruct the temperature and absorption coefficient for Cases 1 and 2 at different *SNRs*. The value of the objective function defined by Eq. (13)

illustrates the convergence of the algorithm and thus can be used to evaluate the performance of the proposed algorithm. Fig. 7 plots them at different iterations. It can be seen that the convergent values are the same for both cases but differ for different noise levels, below 1, 3 and 8 for the corresponding 40, 30 and 20 dB *SNRs*. It is also observed that fewer iterations are required for Case 1 to obtain the minimum convergence value compared to Case 2 at the same *SNR*, meaning that the higher iterations are required for the asymmetry condition to reach minimum convergence. Overall, the values of the objective function with higher iterations indicate better applicability of the hybrid LMBC-NNLS algorithm for both the symmetric and asymmetric conditions.

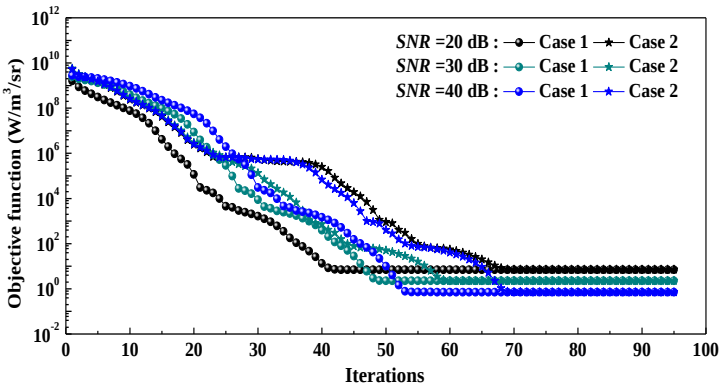

Fig. 7. The values of the objective function with the different iterations and noises.

The relative errors (δT, δK) of the reconstructed temperature and absorption coefficient were calculated to evaluate the reconstruction accuracy of the proposed algorithm. Fig. 8 and Fig. 9 show the calculated relative errors for different noises. The variation of the relative errors is similar for each case. The maximum relative error is observed for the positions Z_r = 4 mm at 16th, 32th and 18th voxels, corresponding to the tip part of the flame because fewer radiative detection lines are received from the tip of the flame. In general, the relative errors are below 10% for all cases at different noise levels, suggesting that the proposed algorithm can reconstruct the temperature and absorption coefficient accurately for both the symmetrical and asymmetrical flames.

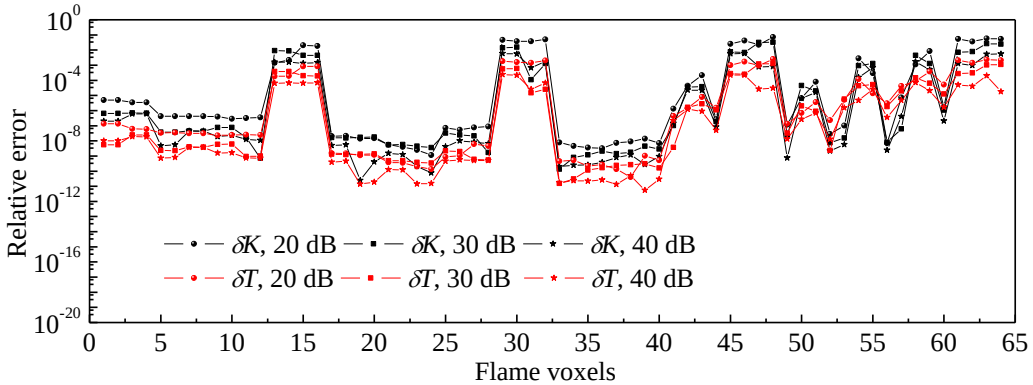

(a) Case 1

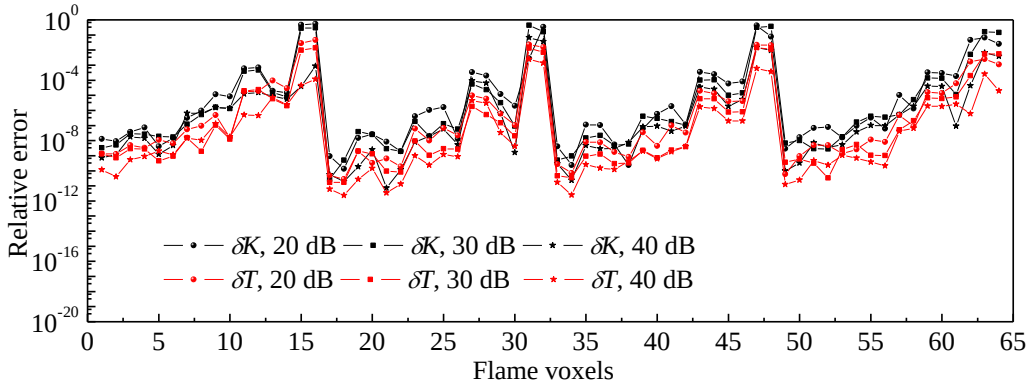

(d) Case 2

Fig. 8. The relative errors of the reconstructed flame temperature and absorption coefficient for different noise levels

The mean relative errors of the temperature and absorption coefficient (ΔT and ΔK) were also calculated, as shown in Fig. 9. In each case, the mean value of ΔK and ΔT increase with *SNR* and thus enlarge the reconstruction errors of T and K. The maximum value of ΔT is below 1% while the maximum value of ΔK is below 10% for all cases, indicating that the flame temperature can be reconstructed more accurately than the absorption coefficient. This coincides with the fact that the radiation intensity is more sensitive to the flame temperature than the absorption coefficient. Moreover, the mean errors become larger for Case 2 due to the asymmetry distribution of the temperature and absorption coefficient.

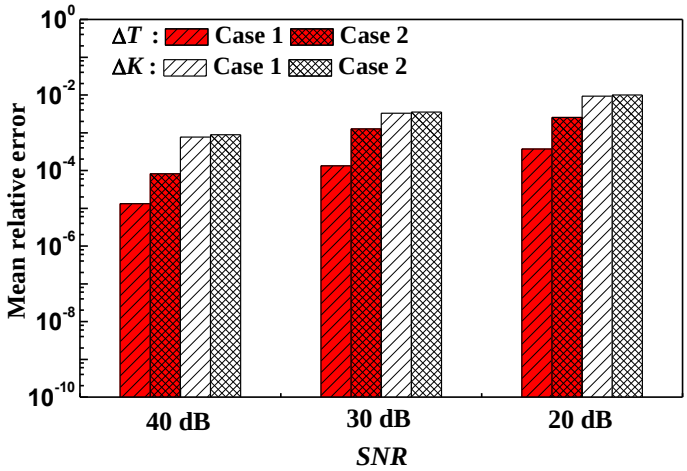

Fig. 9. The mean relative errors of the reconstructed temperature and absorption coefficient for different cases and noises.

The reconstructed distributions of the simulated flame temperature and absorption coefficient when *SNR* = 20 dB are shown in Fig. 10. It can be seen that the reconstructed distributions agree well with the original distributions of flame temperature and absorption coefficient presented in Fig. 3. Better reconstruction of temperature and absorption coefficient was observed for Case 1 in comparison to Case 2. Also, the lower value of ΔT and ΔK was obtained for Case 1. Therefore, the symmetrical distribution of the temperature or absorption coefficient can be reconstructed more accurately than the asymmetrical distribution. The reconstructed results of the simulated flames show that the proposed algorithm is effective for the simultaneous reconstruction of flame temperature and absorption coefficient under the symmetric and asymmetric conditions.

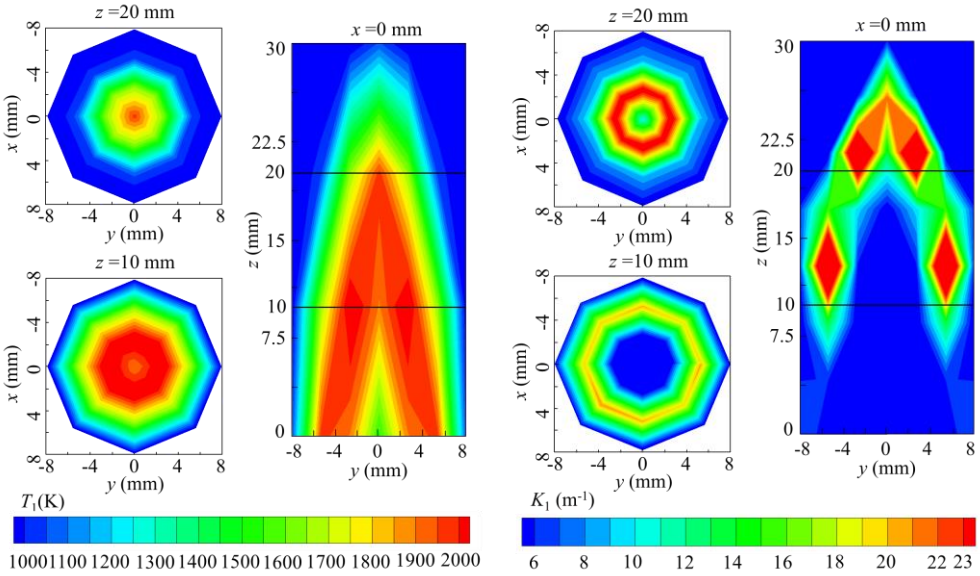

(a) Case 1

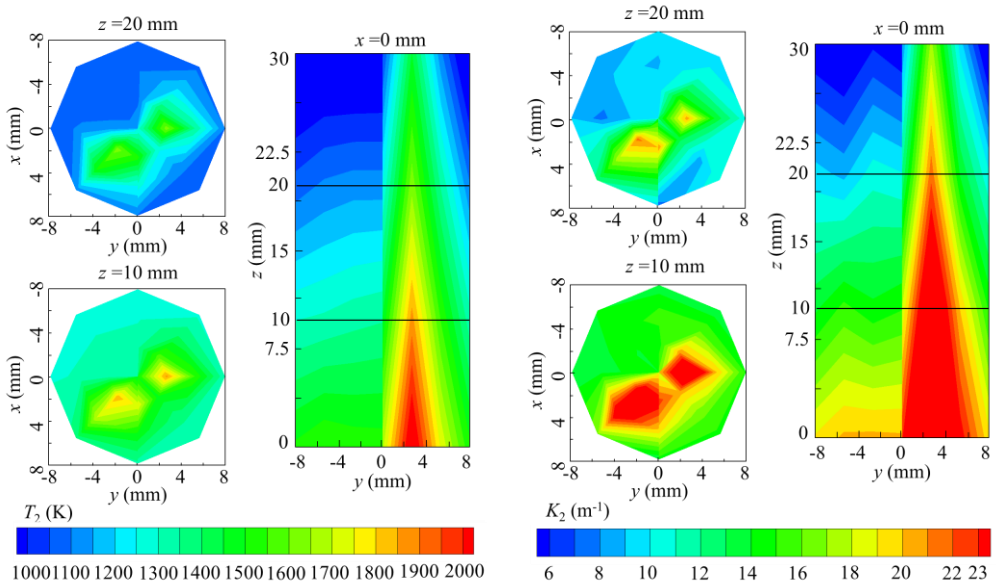

(b) Case 2

Fig. 10. The reconstructed distribution of flame temperature and absorption coefficient for different cases when *SNR* = 20 dB.

4 Experimental research

4.1 Experimental setup

Experiments were conducted to validate the proposed hybrid LMBC-NNLS method. Fig. 11 shows the schematic of the experimental setup. A co-flow burner is used to generate ethylene diffusion flame. The burner consists of two coaxial tubes (i.e., inner and external) with the inner diameters of 10 mm and 50 mm, respectively. The ethylene fuel is supplied through the inner tube and compressed air through the external tube. The co-flow of the ethylene and compressed air is beneficial to stabilize the flame. The flame is shielded by a black painted chamber to eliminate the surrounding disturbance. A colored focused plenoptic camera (Raytrix R29) is utilized to capture the plenoptic flame image and thus to obtain the multi-wavelength flame radiation intensity. The details of the geometric and intensity calibrations have been carried out and reported in previous researches

[7, 43]. The focused plenoptic camera has a 207×160 microlens array. The F-numbers of the main lens and microlens are all F/9.0. The RGB wavelengths of the camera are 610 nm, 530 nm and 460 nm, respectively.

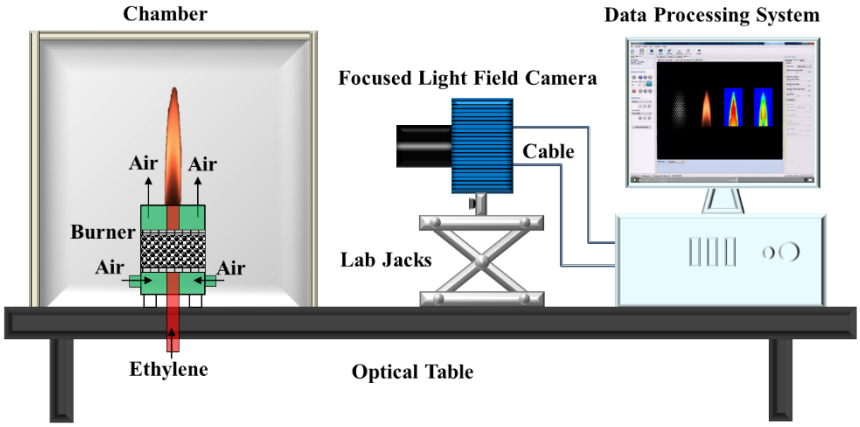

Fig. 11. Schematic of the experimental setup.

During the experiments, six combustion operating conditions (three no co-flow conditions 1, 3 and 5 and three co-flow conditions 2, 4 and 6) were summarized in Table 2 to investigate the reconstruction performance for the proposed hybrid LMBC-NNLS algorithm. Three different ethylene flow rates (0.8, 1.12 and 1.76 mL/s) were considered to analyze the flame temperature and absorption coefficient. Ethylene and air flow pressure were set to 0.2 MPa and 0.5 MPa, respectively. In each condition, 100 raw flame images were captured continuously by the plenoptic camera. Fig. 12 shows typical raw and refocused plenoptic flame images for different experimental conditions. The refocused images were obtained from the captured raw flame images by applying refocusing algorithms described in Ref. [44]. These refocused images can demonstrate the structural shape of the flame. The co-flow of the compressed air squeezes the inner combustion medium and thus the flame shape is a bit thinner compared to the no co-flow conditions.

Table 2. Experimental conditions.

Condition	C_2H_4 (mL/s)	Air (mL/s) (Co-flow)
1	0.8	0
2		138.9
3	1.12	0
4		138.9
5	1.76	0
6		138.9

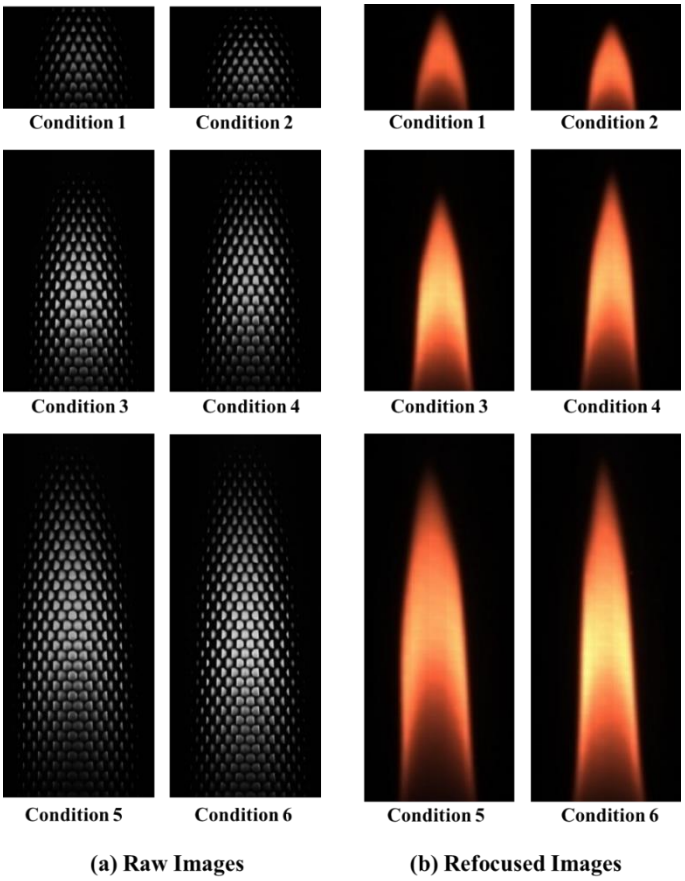

Fig. 12. Example of raw and refocused flame images under different operating conditions.

4.2 Reconstruction of flame temperature and absorption coefficient

To reconstruct the flame temperature, the noise of the CCD sensor was eliminated by subtracting gray levels of the dark image from the raw image. The dark image is captured when the camera is fully capped with no external light. The flame temperature reconstruction is a well-defined ill-posed inverse problem, where the captured radiative rays are the observations and the temperatures of the flame voxels are to be solved. It is observed that the illness of the inverse problem can be reduced by identifying the actual flame area for the reconstruction, which could be achieved by employing a background subtraction algorithm. In this study, an Otsu's thresholding algorithm is used to remove the flame background. Figure 13 illustrates an example of the refocused flame images with and without background for Condition 5.

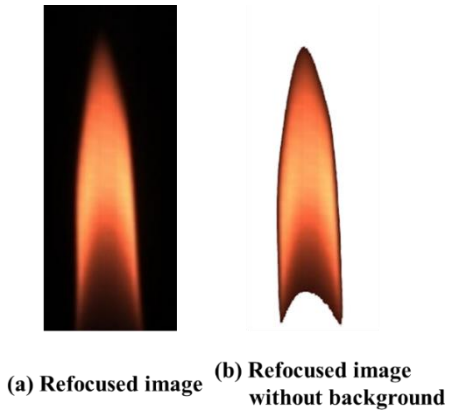

Fig. 13. The refocused flame images with and without background for Condition 5.

The flame was divided into 240 (1 × 20 × 12) voxels in the circumferential (C_r), axial (Z_r) and radial (R_r) directions. The temperature and absorption coefficient of the six conditions were then reconstructed by the proposed LMBC-NNLS. The obtained zero intensity of each flame voxel were interpolated by averaging non-zero values of six neighbourhood flame voxels. The reconstructed results of the flame temperature and absorption coefficient are shown in Fig. 14. The flame temperature varies from about 1200 K to 2000 K. The temperature increases with the ethylene flow rate due to the greater heat release during the combustion reaction. The reconstructed absorption coefficient varies from about 8 m^{-1} to 28 m^{-1}. The absorption coefficient also increases with the ethylene flow rate. This is because the increasing ethylene flow rate would cause a higher flame temperature and thus promote the soot formation. Besides, for the co-flow conditions, more oxygen content diffuses into the fuel, resulting in more intense combustion reaction and heat release. Therefore, the higher temperature and lower absorption coefficient were obtained for the co-flow conditions compared to the no co-flow conditions.

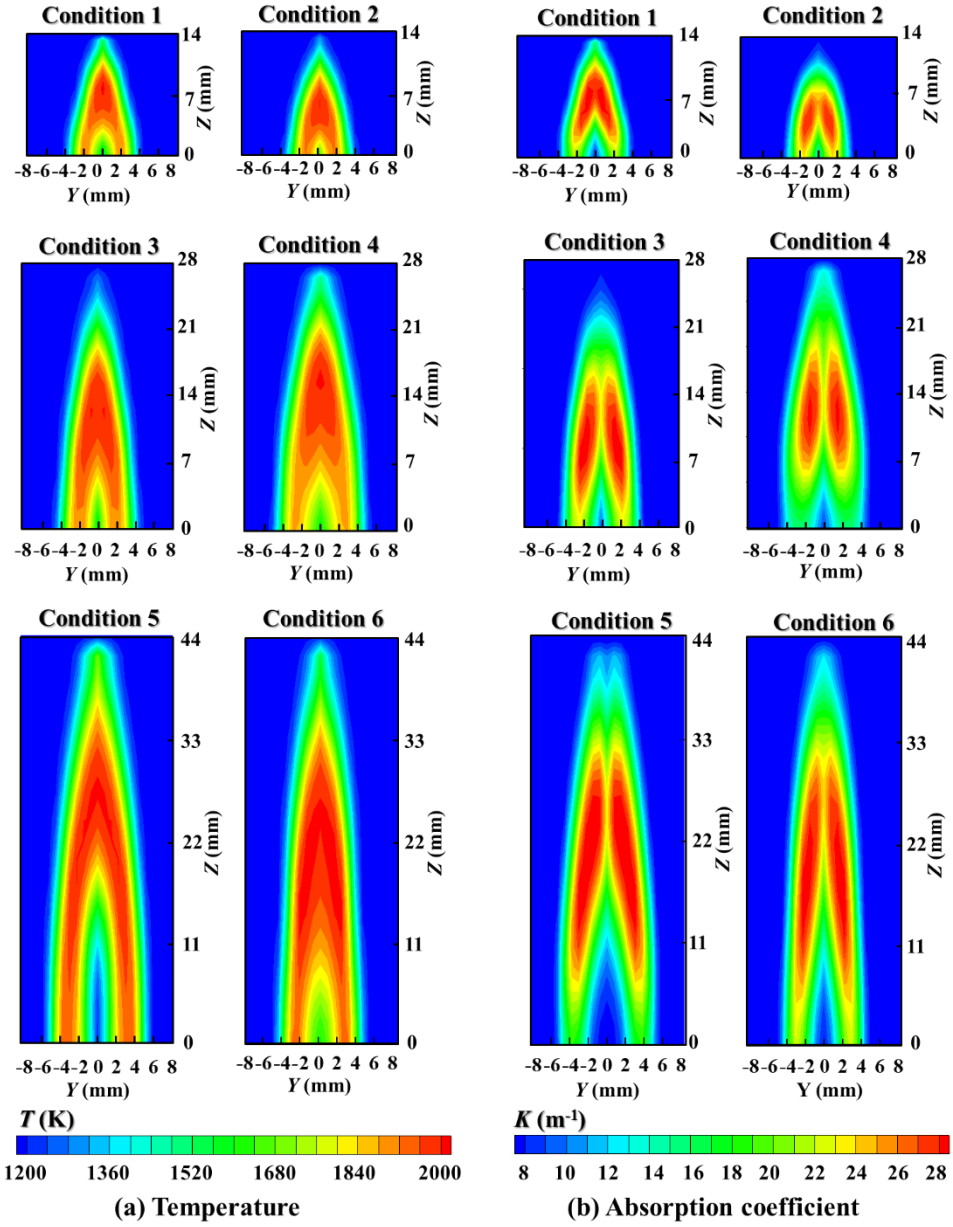

Fig. 14. The reconstructed flame temperature and absorption coefficient over five longitude-sections of the flames under six operating conditions.

During the diffusion and mixing of ethylene and air, the combustion reaction occurs and releases

lots of heat [42]. If the fuel mixture is insufficient, sufficient combustion reaction does not occur in the region closer to the inner of the flame or the region closer to the outside of the flame. In the region with sufficient mixing of fuel and air, the combustion reaction occurs and causes the highest temperature [45]. Besides, soot can be formed in this region during the combustion reaction. For each condition in Fig. 14, the temperature increases first and then decreases from inner to the edge of the flames. The absorption coefficient also has a similar trend as the temperature, but peak at the interior of the peak temperature position. Since the absorption coefficient mainly depends on the soot particles of the flame, the positions of the peak absorption coefficient indicate the positions of plentiful soot formed during the combustion reaction [6]. Moreover, compared to Conditions 1, 3 and 5, the reconstructed shapes of both the temperature and absorption coefficient distribution for co-flow Conditions 2, 4 and 6 are squeezed closer to the flame center, which is consistent with the flame shape in Fig. 12.

4.3 Experimental validation

Further to validate the proposed algorithm, the flame temperature was measured by an R type high precision thermocouple at seven points along the flame diameter (radial axis) over several cross-sections for each experimental condition. Due to the radiation heat loss of the medium to the surroundings and the conduction heat loss of the thermocouple junctions, the measured results of the flame temperature were corrected according to Ref. [4, 46]. Fig. 15 illustrates the comparison between the reconstructed flame temperatures and the thermocouple measurements at five measurement points over three different flame cross-sections. The reconstructed temperatures were averaged from 100 consecutive flame images. A good agreement is demonstrated between the thermocouple measurements and the reconstructed temperatures. It has been observed that the maximum temperature increases with the fuel flow rate although it is difficult to see the difference from Fig. 15 as the maximum temperature point moves with the flame size. Fig. 16 shows the comparison of the reconstructed results with the thermocouple measurement along the central axis of the flame. The flame temperature has peak values along the z-axis for both the LMBC-NNLS and thermocouple measurements. The position of the peak temperature depends on the position of the intense combustion reaction zone and changes with different operating conditions. Also obviously, the flame height increases with the ethylene flow rate. It also can be seen that the maximum difference between the reconstructed and the thermocouple results is 124.2 K (14.3%) at Y = 4 mm and Z = 8 mm (Condition 1). The difference between the two measurements may be explained by the diversity in principle between the two measurement technologies and subtle fluctuation of the flame during the thermocouple measurements. However, a good agreement is observed between the reconstructed results and the thermocouple measurements, demonstrating that the hybrid LMBC-NNLS algorithm is capable of measuring the realistic flame temperature accurately.

It has been realized that the radiative information recorded by the single plenoptic camera is limited due to the limited viewing angle and it is a common restraint of the single plenoptic camera for the flame temperature measurement. As a result, the resolution of the reconstructed flame temperature is quite low, only 1 × 20 × 12 in the circumferential (C_r), axial (Z_r) and radial (R_r) directions in this study. In the experiments, subtle temperature changes, especially in the flame sheet, cannot be observed in the reconstructed flame temperature. Instead, wider distributions of high temperature are obtained as the flame sheet occupies only a small part of the voxel.

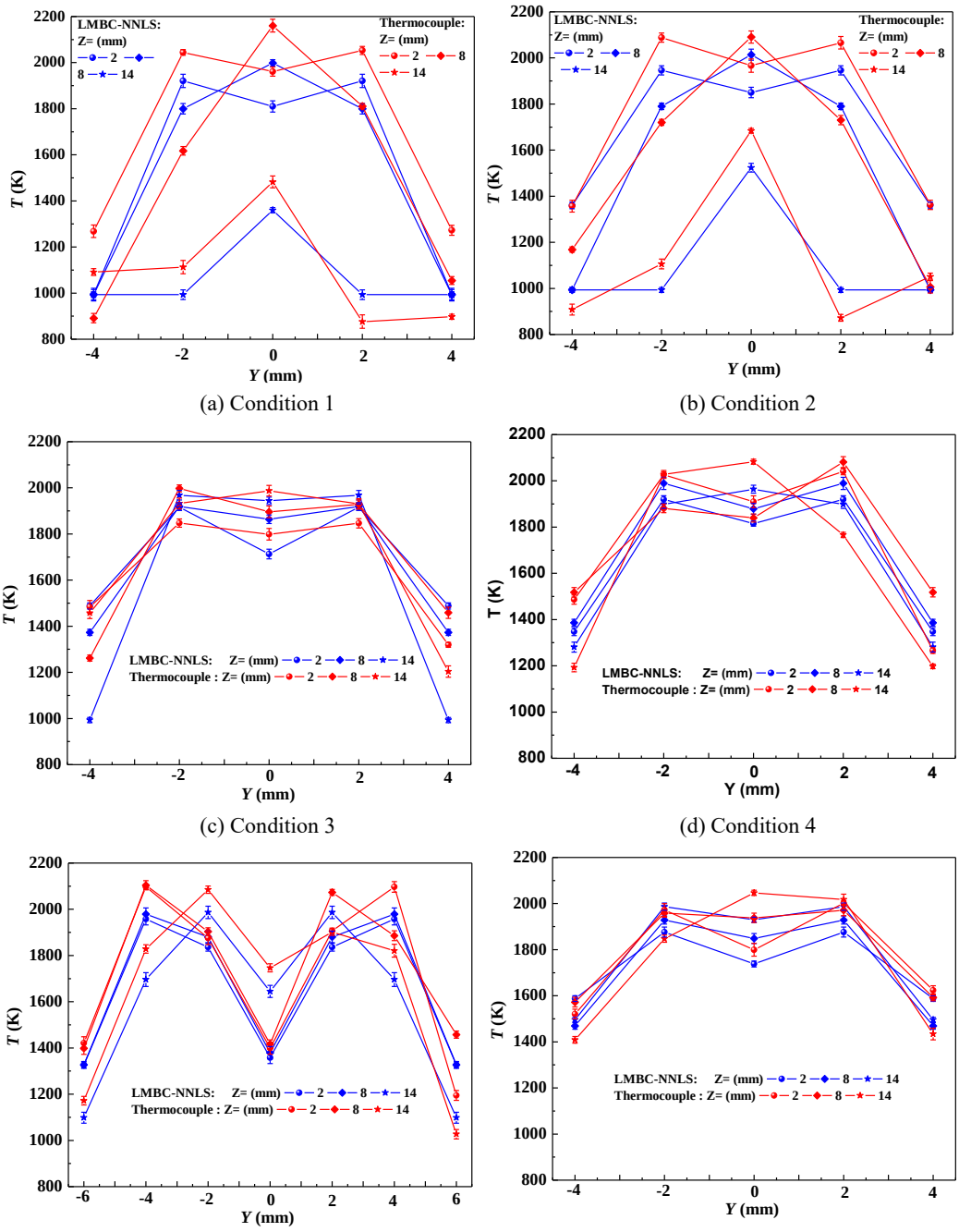

(a) Condition 1 (b) Condition 2

(c) Condition 3 (d) Condition 4

(e) Condition 5 (f) Condition 6

Fig. 15. The comparison between the reconstructed flame temperatures and the thermocouple measurements at five measurement points over three flame cross-sections.

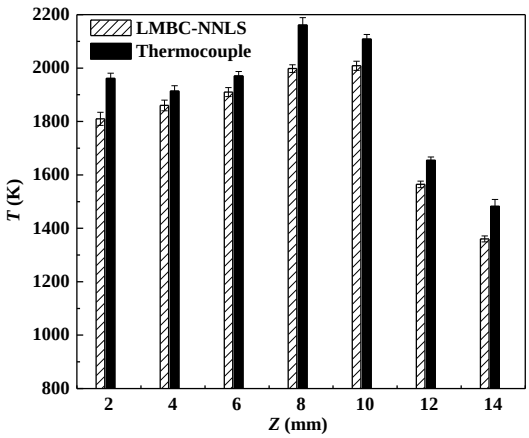

(a) Condition 1

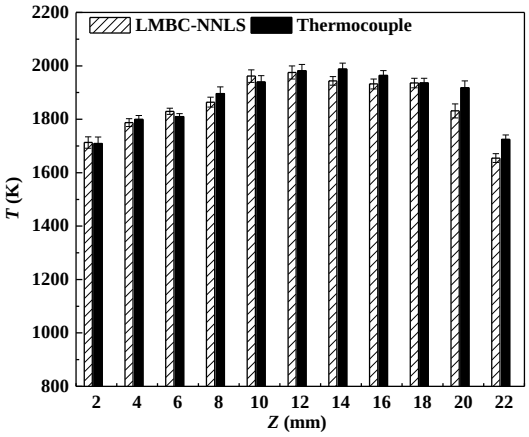

(b) Condition 3

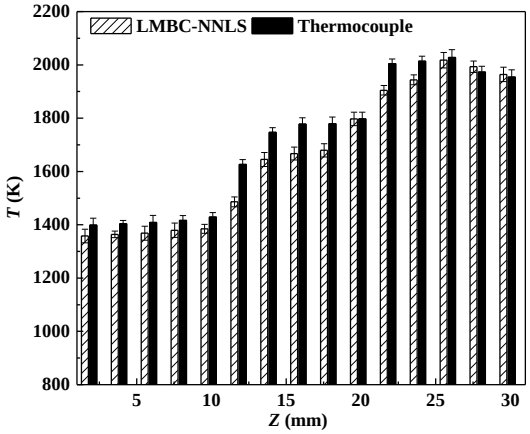

(c) Condition 5

Fig. 16. The comparison of the reconstructed results with the thermocouple measurement along the central axis of the flame.

It is worth noting that the Otsu's thresholding method cannot determine the root part of the flame boundary accurately. Thus, there are some errors involved in the reconstruction of the flame root part. Therefore, the flame boundary treatment needs to be further improved. In addition, other factors may also contribute to the measurement errors in this study such as the geometric calibration error. The geometric calibration error could cause the inaccurate calculation of the direction and starting position of the detection ray. The calibration errors are up to 0.2% found in our previous study [41]. Generally, the above results demonstrate that the proposed algorithm is capable of reconstructing the flame temperature and absorption coefficient successfully.

5. Conclusions

In this paper, the hybrid LMBC-NNLS algorithm was proposed to reconstruct the flame temperature and absorption coefficient simultaneously based on plenoptic imaging technique. Numerical simulations were carried out for the symmetric and asymmetric distribution of the flame temperature and absorption coefficient to validate the proposed algorithm. Experiments were also carried out on the ethylene diffusion flames and the flame temperature and absorption coefficient were simultaneously reconstructed using the LMBC-NNLS algorithm. The obtained temperature was also compared with the thermocouple measurements. The concluding remarks are as follows:

(1) It has been observed that the negative values of the radiation intensity and absorption coefficient can be generated in the reconstruction using the inverse algorithms such as LMBC-LSQR and

LM-NNLS without boundary constraint. The proposed hybrid LMBC-NNLS algorithm is effective to simultaneously reconstruct the flame temperature and absorption coefficient without generating negative values, and thus with improved reconstruction accuracy.

(2) The reconstruction errors of the flame temperature and absorption coefficient with the proposed algorithm are all below 10% for both the symmetric and asymmetric cases according to the numerical simulations, demonstrating the proposed algorithm can reconstruct the flame temperature and absorption coefficient simultaneously under different combustion conditions.

(3) Experiments on a co-flow burner are carried out to reconstruct the flame temperature and absorption coefficient simultaneously. A good agreement between the reconstructed result and the thermocouple measurement was observed with a maximum difference of 124.2 K, proving the feasibility of the proposed hybrid LMBC-NNLS algorithm.

Acknowledgements

This work was supported by the National Natural Science Foundation of China (51676044, 51506030, 51327803) and the Natural Science Foundation of Jiangsu Province for Distinguished Young Scholars (BK20150023).

References

1. H. Yi, X. Guo, J. Hao, L. Duan and X. Li. *Characteristics of inhalable particulate matter concentration and size distribution from power plants in China.* Journal of the Air & Waste Management Association, 2006, 56(9): 1243-1251.
2. S. Javadi, and M. Moghiman. *Experimental study of natural gas temperature effects on the flame luminosity and NO emission.* International Journal of Spray and Combustion Dynamics, 2012, **4**(2): 175-184.
3. H. Zhou, X. Lou, and Y. Deng. *Measurement method of three-dimensional combustion temperature distribution in utility furnaces based on image processing radiative.* Proceedings of the CSEE, 1997, **17**(1): 1-4.
4. M. M. Hossain, G. Lu, D. Sun and Y. Yan. *Three-dimensional reconstruction of flame temperature and emissivity distribution using optical tomographic and two-colour pyrometric techniques.* Measurement Science and Technology, 2013, **24**(7): 1-10.
5. X. Huang, H. Qi, C. Niu, L. Ruan, H. Tan, J. Sun and C. Xu. *Simultaneous reconstruction of 3D temperature distribution and radiative properties of participating media based on the multi-spectral light-field imaging technique.* Applied Thermal Engineering, 2017, **115**: 1337-1347.
6. H. Liu, S. Zheng and H. Zhou. *Measurement of Soot Temperature and Volume Fraction of Axisymmetric Ethylene Laminar Flames Using Hyperspectral Tomography.* IEEE Transactions on Instrumentation and Measurement, 2017, **66**(2): 315-324.
7. J. Sun, C. Xu, B. Zhang, M. M. Hossain, S. Wang, H. Qi and H. Tan. *Three-dimensional temperature field measurement of flame using a single light field camera.* Optics express, 2016, **24**(2): 1118-1132.
8. H. Yang, B. Yang, X. CAI, C. Hecht, T. Dreier and C. Schulz. *Three-Dimensional (3-D) Temperature Measurement in a Low Pressure Flame Reactor Using Multiplexed Tunable Diode Laser Absorption Spectroscopy (TDLAS).* Lasers in Engineering (Old City Publishing), 2015, **31(5/6): 285-297**.
9. S. Someya, Y. Okura, T. Munakata and K. Okamoto. *Instantaneous 2D imaging of temperature in an engine cylinder with flame combustion.* International Journal of Heat and Mass Transfer, 2013, **62**: 382-390.
10. V. Hindasageri, R. P. Vedula and S. V. Prabhu. *Thermocouple error correction for measuring the*

flame temperature with determination of emissivity and heat transfer coefficient. Review of Scientific Instruments, 2013, **84**(2): 024902-1-12.

11. U. Stopper, M. Aigner, H. Ax, W. Meier, R. Sadanandan, M. Stöhr and A. Bonaldo. *PIV, 2D-LIF and 1D-Raman measurements of flow field, composition and temperature in premixed gas turbine flames.* Experimental Thermal and Fluid Science, 2010, **34**(3): 396-403.
12. D. Müller, R. Pagel, A. Burkert, V. Wagner and W. Paa. *Two-dimensional temperature measurements in particle loaded technical flames by filtered Rayleigh scattering.* Applied optics, 2014, **53**(9): 1750-1758.
13. X. Zhang, Q. Cheng, C. Lou and H. Zhou. *An improved colorimetric method for visualization of 2-D, inhomogeneous temperature distribution in a gas fired industrial furnace by radiation image processing.* Proceedings of the Combustion Institute, 2011, **33**(2): 2755-2762.
14. T. S. Draper, D. Zeltner, D. R. Tree, Y. Xue and R. Tsiava. *Two-dimensional flame temperature and emissivity measurements of pulverized oxy-coal flames.* Applied Energy, 2012, **95**: 38-44.
15. C. Xu, W. Zhao, J. Hu, B. Zhang and S. Wang. *Liquid lens-based optical sectioning tomography for three-dimensional flame temperature measurement.* Fuel, 2017, **196**: 550-563.
16. J. Doi, and S. Sato. *Three-dimensional modeling of the instantaneous temperature distribution in a turbulent flame using a multidirectional interferometer.* Optical Engineering, 2007, **46**(1): p. 015601-1-7.
17. M. M. Hossain, G. Lu and Y. Yan. *Optical fiber imaging based tomographic reconstruction of burner flames.* IEEE Transactions on Instrumentation and Measurement, 2012, **61**(5): 1417-1425.
18. M. Ni, H. Zhang, F. Wang, Z. Xie, Q. Huang, J. Yan and K. Cen. *Study on the detection of three-dimensional soot temperature and volume fraction fields of a laminar flame by multispectral imaging system.* Applied Thermal Engineering, 2016, **96**: 421-431.
19. Y. Gong, Q. Guo, Q. Liang, Z. Zhou and G. Yu. *Three-dimensional temperature distribution of impinging flames in an opposed multiburner gasifier.* Industrial & Engineering Chemistry Research, 2012, **51**(22): 7828-7837.
20. H. Zhou, C. Lou, Q. Cheng, Z. Jiang, J. He, B. Huang, Z. Pei and C. Lu. *Experimental investigations on visualization of three-dimensional temperature distributions in a large-scale pulverized-coal-fired boiler furnace.* Proceedings of the Combustion Institute, 2005, **30**(1): 1699-1706.
21. L. Ma, W. Cai, A. W. Caswell, T. Kraetschmer, S. T. Sanders, S. Roy and J. R. Gord. *Tomographic imaging of temperature and chemical species based on hyperspectral absorption spectroscopy.* Optics Express, 2009, **17**(10): 8602-8613.
22. Q. Huang, F. Wang, D. Liu, Z. Ma, J. Yan, Y. Chi and K. Cen. *Reconstruction of soot temperature and volume fraction profiles of an asymmetric flame using stereoscopic tomography.* Combustion and Flame, 2009, **156**(3): 565-573.
23. P. M. Brisley, G. Lu, Y. Yan and S. Cornwell. *Three-dimensional temperature measurement of combustion flames using a single monochromatic CCD camera.* IEEE transactions on instrumentation and measurement, 2005, **54**(4): 1417-1421.
24. H. Wang, Z. Huang, D. Wang, Z. Luo, Y. Sun, Q. Fang, C. Lou and H. Zhou. *Measurements on flame temperature and its 3D distribution in a 660 MWe arch-fired coal combustion furnace by visible image processing and verification by using an infrared pyrometer.* Measurement Science & Technology, 2009, **20**(11): 114006-1-12.
25. X. Zhang, S. Zheng, H. Zhou, B. Zhang, H. Wang and H. Xu. *Simultaneously reconstruction of*

inhomogeneous temperature and radiative properties by radiation image processing. International Journal of Thermal Sciences, 2016, **107**: 121-130.

26. N. Anfimov, G. Karabadyak, B. Khmelinin, Y. Plastinin and A. Rodionov. *Analysis of mechanisms and the nature of radiation from aluminum oxide in different phase states in solid rocket exhaust plumes*. In *28th Thermophysics Conference*, 1993.
27. R. Reed and V. Calia. *Review of aluminum oxide rocket exhaust particles*. In *28th Thermophysics Conference*, 1993.
28. W. Fiveland. *Three-dimensional radiative heat-transfer solutions by the discrete-ordinates method.* Journal of Thermophysics and Heat Transfer, 1988, **2**(4): 309-316.
29. C. Lou and H. Zhou, *Assessment of regularized reconstruction of three-dimensional temperature distributions in large-scale furnaces.* Numerical Heat Transfer, Part B: Fundamentals, 2008, **53**(6): 555-567.
30. D. Liu, J. Yan, F. Wang, Q. Huang, Y. Chi and K. Cen. *Experimental* reconstructions *of flame temperature distributions in laboratory-scale and large-scale pulverized-coal fired furnaces by inverse radiation analysis.* Fuel, 2012, **93**(1): 397-403.
31. D. Liu, Q. Huang, F. Wang, Y. Chi, K. Cen and J. Yan. *Simultaneous Measurement of Three-Dimensional Soot Temperature and Volume Fraction Fields in Axisymmetric or Asymmetric Small* Unconfined *Flames With CCD Cameras.* Journal of Heat Transfer, 2010, **132**(6):061202-1-7.
32. C. Niu, H. Qi, X. Huang, L. Ruan, W. Wang and H. Tan. *Simultaneous reconstruction of temperature distribution and radiative properties in participating media* using *a hybrid LSQR–PSO algorithm.* Chinese Physics B, 2015, **24**(11): 114401.
33. C. Niu, H. Qi, X. Huang, L. Ruan and H. Tan. *Efficient and robust method for simultaneous reconstruction of the temperature distribution and radiative properties in absorbing, emitting, and scattering media.* Journal of Quantitative Spectroscopy and Radiative Transfer, 2016, **184**: 44-57.
34. T. Li, S. Li, Y. Yuan, F. Wang and H. Tan. *Light field imaging analysis of flame radiative properties based on Monte Carlo method.* International Journal of Heat and Mass Transfer, 2018, **119**: 303-311.
35. H. Huang, and Y. Zhang. *Flame colour characterization in the visible and infrared spectrum using a digital camera and image processing.* Measurement Science and Technology, 2008, **19**(8): p. 085406-1-9.
36. O. Johannsen, C. Heinze, B. Goldluecke and C. Perwaß. *On the Calibration of Focused Plenoptic Cameras*. *Time-of-Flight and Depth Imaging*. Sensors, Algorithms, and Applications. Springer, Berlin, Heidelberg, 2013. 302-317.
37. J. D. Felske and C. L. Tien, *Calculation of the* emissivity *of luminous flames.* Combustion Science and Technology, 1973, **7**(1): 25-31.
38. C. L. Lawson and R. J. Hanson. *Solving least squares* problems. SIAM, 1995.
39. K. Levenberg. *A method for the solution of certain non-linear problems in least squares.* Quarterly of applied mathematics, 1944, **2**(2): 164-168.
40. D. W. Marquardt. *An algorithm for least-squares estimation of nonlinear parameters.* Journal of the society for Industrial and Applied Mathematics, 1963, **11**(2): 431-441.
41. J. M. Bardsley. *A Bound-Constrained Levenburg-Marquardt Algorithm for a Parameter Identification Problem in Electromagnetics.* University of Montana, 2004: 6-13..

42. R. J. Santoro, T. T. Yeh, J. J. Horvath and H. G. Semerjian. *The Transport and Growth of Soot Particles in Laminar Diffusion Flames.* Combustion Science & Technology, 1987, **53**(2-3): 89-115.
43. J. Sun, M. M. Hossain, C. Xu, B. Zhang and S. Wang. *A novel calibration method of focused light field camera for 3-D* reconstruction *of flame temperature.* Optics Communications, 2017, **390**: 7-15.
44. R. Ng, M. Levoy, M. Brédif, G. Duval, M. Horowitz and P. Hanrahan. *Light field photography with a hand-held plenoptic camera.* Computer Science Technical Report CSTR, 2005, **2**(11): 1-11.
45. S. R. Turns. *An* introduction *to combustion*. New York: McGraw-hill, 1996.
46. C. S. McEnally, Ü. Ö. Köylü, L. D. Pfefferle and D. E. Rosner. *Soot volume fraction and temperature measurements in laminar nonpremixed flames using thermocouple*. Combustion and Flame, 1997, 109(4): 701-720.